Tuning Piezoelectricity via Thermal Annealing at a Freestanding Ferroelectric Membrane

*Lu Han[1, 2, ‡], Xinrui Yang[1, 2, ‡], Yingzhuo Lun[3, ‡], Yue Guan[1, 2], Futao Huang[1, 2], Shuhao Wang[4], Jiangfeng Yang[1, 2], Chenyi Gu[1, 2], Zheng-Bin Gu[1, 2], Lisha Liu[4], Yaojin Wang[4], Peng Wang[1, 2, 5], Jiawang Hong[3, *], Xiaoqing Pan[6, 7, 8], & Yuefeng Nie[1, 2, *]*

[1]National Laboratory of Solid State Microstructures, Jiangsu Key Laboratory of Artificial Functional Materials, College of Engineering and Applied Sciences, Nanjing University, Nanjing 210093, P. R. China.

[2]Collaborative Innovation Center of Advanced Microstructures, Nanjing University, Nanjing 210093, P. R. China.

[3]School of Aerospace Engineering, Beijing Institute of Technology, Beijing 100081, P. R. China.

[4]School of Materials Science and Engineering, Nanjing University of Science and Technology, Nanjing 210094, Jiangsu, P. R. China.

[5]Department of Physics, University of Warwick, Coventry CV4 7AL, UK.

[6]Department of Physics and Astronomy, University of California, Irvine, CA 92697, USA.

[7]Department of Materials Science and Engineering, University of California, Irvine, CA 92697, USA.

[8]Irvine Materials Research Institute, University of California, Irvine, CA 92697, USA.

KEYWORD. Freestanding complex oxide, ferroelectric perovskite oxide, piezoelectric, molecular beam epitaxy, lead titanate ($PbTiO_3$)

ABSTRACT

Tuning the ferroelectric domain structure by a combination of elastic and electrostatic engineering provides an effective route for enhanced piezoelectricity. However, for epitaxial thin films, clamping effect imposed by the substrate does not allow aftergrowth tuning and also limits the electromechanical response. In contrast, freestanding membranes, which are free of substrate constraints, enable the tuning of subtle balance between elastic and electrostatic energies, giving new platforms for enhanced and tunable functionalities. Here, highly tunable piezoelectricity is demonstrated in freestanding $PbTiO_3$ membranes, by varying the ferroelectric domain structures from *c*-dominated to *c*/*a* and *a* domain via aftergrowth thermal treatment. Significantly, the piezoelectric coefficient of the *c*/*a* domain structure is enhanced by a factor of 2.5 compared with typical *c* domain $PbTiO_3$. This work presents a new strategy to manipulate the piezoelectricity in ferroelectric membranes, highlighting their great potential for nano actuators, transducers, sensors and other NEMS device applications.

TEXT

Piezoelectrics interconvert mechanical energy and electric charge[1], which is crucial for applications such as sensors, transducers, resonators and actuators[2-4]. As piezoelectric devices continue to be miniaturized, low-/two-dimensional (2D) nanomaterials with excellent longitudinal piezoelectricity are highly sought-after[5, 6]. Besides, the easily-stackable nature makes them integrable with highly dissimilar materials by van-der-Waals (vdW) interactions, such as industrial silicon substrates or flexible layers, compatible with existing technological platforms. To address this, 2D piezoelectric material is a natural choice, however, the magnitude of the out-of-plane (OOP) piezoelectric component (referred to as d_{33}) has been estimated to be several picometers per volt, rather small for practical use in piezotronics[7-9]. On the other hand, ferroelectric perovskite oxide materials can exhibit a much higher piezoelectric charge coefficient[10]. Synthesizing nanoscale films on single-crystal oxide substrates is a traditional approach to reduce the dimension, whereby the piezoelectric properties can be precisely engineered at the atomic level. Despite the superior performance, epitaxial systems cannot stand without substrates, which sets further limitations on applications regarding to isolated 2D layers[11] or vdW heterogenous integration[6]. Recently-developed freestanding perovskite oxide film that can be made down to the monolayer limit provides a new quasi-2D system with large piezoelectric response for nanoscale piezoelectric devices[12, 13].

In ferroelectrics, large responses tend to arise at a phase boundary between several nearly energetically degenerate phases (i.e., morphotropic phase boundaries, MPBs) where interconversion of phases is possible by external stimuli[14, 15]. In a similar vein, the domain-structure instability and competition in epitaxial films also provide a route to large electromechanical responses. For instance, in $BiFeO_3$, the coexistence of tetragonal- and rhombohedral-like phases

can be driven by modern strain-engineering routes, accompanied with large electromechanical strains[16, 17]. Even in single-phase $PbTiO_3$ (PTO) films, a strain-induced domain-structure competition also gives rise to large responses[18]. Whereas epitaxial ferroelectric films are ideal to control structure-properties relationships, the clamping effect imposed by the substrate has severe limitations: 1) As the planar strain is fixed to the substrate lattice, it is difficult to rearrange the domain structures in epitaxial film once grown on selected substrates, which puts a hard constraint on aftergrowth tuning of its piezoelectricity; 2) Substrates govern the elastic response of the system, limiting piezoelectric deformations upon application of external electric field. In contrast, freestanding membranes, which are free of substrate constraints, giving new platforms for enhanced and tunable functionalities[19-23]. Despite these advantages, it is still an open question how to engineer domain structures and thus the related piezoelectric properties in freestanding films after integrated on silicon.

Here, we report a novel thermal treatment to modulate domain structures in freestanding PTO membranes that gives rise to highly tunable longitudinal piezoelectricity. After annealing with different cooling rates, domain structures undergo a transition from an original OOP *c*-dominated domain to a *c*/*a* domain and an in-plane (IP) polarized *a* domain structure. Strikingly, the piezoelectric coefficient of *c*/*a* domain structure (~214 pm/V) is enhanced by a factor of 2.5 compared with original *c*-dominated domain state. These results offer a route to achieve low-dimensional ferroelectric materials with tunable electromechanical properties, with broader perspectives for M/NEMS device applications.

Instead of following common strain-engineering routes[24-26], we manipulate domain structures of the freestanding PTO films via an aftergrowth thermal treatment. The logic of our approach is given in Fig. 1a and the most energetically favorable direction of polarization can be revealed from

the minima of free energy surface as function of polarization direction (Fig. S1)[27]. For as-grown state, the PTO film is compressively strained on STO substrate before released, the preferable direction of polarization is out-of-plane (Fig. 1a, i). When releasing the film from the substrate (Fig. 1a, ii), the energy surface remains unchanged corresponding to a *c* domain structure (note that for bulk PTO with *c* domain, the in-plane lattice constant is nearly similar to that of STO), which indicates the transferring process barely influences the domain structures. Above Curie temperature, PTO has a paraelectric cubic pahse (Fig. 1a, iii). During the cooling process, PTO forms ferroelectric tetragonal phases. Due to the depolarization field, the *c* domain with polarization along the out-of-plane direction is metastable since they are energetically less favorable than the *a* domain with polarization along the out-of-plane directions (Fig. 1a, iv). If the cooling rate is slow, the PTO will form pure *a* domains since they are a global ground states (Fig. 1a, v). In contrast, if the cooling rate is fast, a "glassy" state can be formed and part of the films will be relaxed to the metastable *c* domain state (Fig. 1a, vi). As such, the effective average in-plane lattice constants varies with the cooling rate.

Analytical phenomenological and phase-field models have been employed to understand, predict and design domain structures in numerous ferroelectrics[28-30]. Here we employ the phase-field method to reveal the domain evolution and calculate the longitudinal piezoelectric coefficient d_{33} for PTO[31]. Details of calculations are provided in Methods. The piezoelectric response was calculated by applying a small probing electrical field to the stable relaxed domain structures along the OOP direction. The corresponding average OOP strain is used to evaluate the piezoelectric coefficient d_{33} by dividing it with the applied electric field. As illustrated in Fig. 1b, the piezoelectric coefficient d_{33} is mainly determined by the domain structures. The greatest piezoelectric performance is obtained in the coexistence of *c* and *a* domain. The piezoelectricity

gradually becomes weakened as the fraction of *c*/*a* domain decreases. In addition, the monodomain *c* exhibits higher piezoelectricity than the monodomain *a*. The enhanced piezoelectric performance is related to the increased *c*/*a* domain wall (DW) density (Fig. 1b and Fig. S2b, c) because these ferroelastic domain walls lead to the ease of polarization rotation[32-34], thus significantly contributing to piezoelectric properties.

To validate the above concept, we firstly investigate the structural evolution after heating and slowly cooling (20 °C/min) the freestanding PTO membranes in air. By reactive molecular beam epitaxy (MBE), we synthesized 6 u.c. $Sr_3Al_2O_6$ (SAO) and 50 nm PTO films on (001) $SrTiO_3$ (STO) and then transferred to desired substrates by dissolving SAO layer via water. Possible impact of hydroxyl during the water treatment and annealing has been checked using X-ray photoemission spectroscopy (XPS) measurements (Fig. S3), indicating that the hydroxyl plays a minor role in the energy of the system. More details about the film growth, transfer and characterization can be found in Methods and Fig. S4.

To reveal structural evolution, high-resolution transmission electron microscopy and *in-situ* XRD measurement are used to characterize the crystal structures. Atomic-resolution plane-view HAADF images of freestanding PTO film before and after annealing show the polarization along the [001] and [100] direction, respectively (Fig 2a, b). Schematic projective views of the unit-cell of ferroelectric PTO along the [001] direction (ii) and the [100] direction (iii) indicate the crystal structures. A charge dipole forms in the PTO unit-cell due to the separation of positive and negative electric center, which defines the vector direction of spontaneous polarization P_s (along opposite displacement of Ti^{4+}, parallel to $[00\bar{1}]$). The displacement of Ti^{4+} cannot be observed in the projection of the unit-cell along the [001] direction (Fig. 2a, iii), while the displacement of Ti^{4+}

can be clearly seen in the HAADF images of annealed sample (Fig. 2b, iii), which indicates the direction of polarization turns from OOP into IP direction after annealed with low cooling rate.

Moreover, the high-resolution X-ray diffraction (HRXRD) measurement is conducted on freestanding PTO films (50 nm) to explore the structural evolution during annealing processes. The transferred freestanding PTO films before annealed is *c*-dominated domain structure which is consistent with the STEM results. Fig. 2c shows 2θ-ω scans around PTO (002) peak during annealing, accompanied with the corresponding variation of out-of-plane lattice parameters (Fig. 2d). Within the whole heating temperature range (25 to 500°C), the OOP lattice parameter decreases and it suddenly changes from 4.05 Å (450°C) to about 3.96 Å (500°C), demonstrating that a phase transition from room-temperature tetragonal phase to high-temperature cubic phase[31].

For traditional epitaxial PTO films clamped by substrate, during cooling process, it exhibits an increase of OOP lattice parameter (Fig. S5a-d). Besides, it can be clearly seen that with the decrease of film thickness, the T_c of PTO film on substrate also decrease, which is related to the existence of depolarizing field (Fig. S5e). However, strikingly different effect is observed in freestanding films. When subsequently cooling the freestanding samples, unlike situations in films clamped by substrate (the diffraction peaks shift back to lower 2θ values), the diffraction peaks continuously shift to higher 2θ values, indicating a decrease of the average OOP lattice parameter, down to 3.921 Å at room temperature (Fig. 2c, d). The reduced OOP lattice parameter suggests that the longer *c*-axis and hence the polarization both switch from out-of-plane to in-plane direction. To further investigate the crystal structure after annealing, each lattice parameter for both a_1 and a_2 domains is defined and plotted in Fig. S6. Therefore, both the STEM and HRXRD results demonstrate that during low-rate annealing, the OOP lattice shrinks and the IP lattice

expands, resulting in an evolution from original *c*-dominated domain structure to in-plane *a* (a_1/a_2) domain structure.

The domain structures in freestanding PTO films are dramatically affected by the cooling rate. As discussed above, the as-released freestanding film possesses *c*-dominated domain structure before annealed (Fig. 3a). When the cooling rate is low enough (20°C/min), it prefers to form *a* domain structure (Fig. 3c) due to the dominated impact of the electrostatic energy. However, when a higher cooling rate of 50°C/min is applied to the sample, the internal strain cannot be fully released, resulting in the elastic and electrostatic forces compete with each other and forming a different domain structure. As shown in Fig. 3b, the domain structures reflect a *c*/*a* domain structure. Unlike classic *c*/*a* twins reported in epitaxial PTO films[35, 36], these structures show more complicated features with both 90° *c*/*a* and 180° *c*+/*c*- domain walls (Fig. S7).

Moreover, the ferroelectric switching behaviors of these three distinct domain structures have also been investigated. For as-released freestanding PTO film, the polarization state of $2 \times 2\ \mu m^2$ region with +10 V sample bias is similar to the transferred region, indicating that the transferred freestanding film has a downward ferroelectric polarization (Fig. 3d). The ferroelectric polarization in freestanding films is the same as it is in the as-prepared samples (Fig. S8). The switching behavior of freestanding PTO film with *c*/*a* domain is shown in Fig. 3e. The domain switching region shown in vertical PFM (VPFM) amplitude and phase images indicates that the polarization can be switched from IP to OOP direction (Fig. 3e). For the in-plane *a* domain structure (Fig. 3f), the polarization pointing to the IP direction can also be switched via trailing field[26, 37, 38]. An in-plane electric field is available by applying a bias between the bottom electrode and a metallic AFM tip. During the switching, the bias is applied to the tip while scanning the film in the [100] direction (from left to right of the picture) or in the [$\bar{1}$00] direction (from right to left

of the picture), leading to an effective electric trailing field along opposite in-plane directions shown in Fig. 3f.

These typical domain structures and corresponding switching behaviors demonstrate that we have the ability to control different domain patterns in freestanding PTO film on silicon and it preserves a relatively good ferroelectricity. It should be noted that, domain structure engineering is accompanied with change of average in-plane lattice constant, which might make the film wrinkled at the macroscale. To avoid this, etching the freestanding films into small pieces in advance might be helpful.

Having manipulating domain structures in the same 50 nm freestanding PTO films, we now discuss their electromechanical response based on PFM measurements, which has been widely applied for quantifying piezoelectric coefficient d_{33} where small displacements are involved[39, 40]. In PFM measurements, an AC signal is first applied between a conducting atomic force microscope (AFM) tip and a bottom contact electrode. Next, the AFM tip is brought into contact with the surface. Finally, the electromechanical response of the surface is detected as optically mapped deflections of the tip[41]. In order to detect the electromechanical response of films with dominated-*c*, *c*/*a* and *a* domain structures, the data are collected on a 3 × 3 grid of points over 3 × 3 μm^2 region of each film shown in Fig. 4a-c. More details about the domain structures can be found in Fig. S9. Notably, the tested AC voltage used in our PFM measurements is low enough (less than 3V) to make sure there is no irreversible domain structure conversion happened, thus it is a true representation of PTO piezoresponse[42]. In order to ensure that the tested voltage is lower than the coercive field, we do the OOP domain switching shown in Fig. S10, indicating that a voltage less than 3V cannot change the domain structure.

In this study, 9 array points are chosen uniformly to reflect piezoelectric response of freestanding PTO films, those are as-released (*c*-dominated domain), after fast cooling (*c*/*a* domain) and slow cooling (*a* domain) samples. During the test, the AC amplitude is ramped from 1 to 3 V (0 V DC bias) while the tip is held at one point. The representative piezoelectric displacement (Z_{eff}) of 9 array points on the freestanding film, as functions of the applied AC tip bias are shown in Fig. 4d-f. Finally, the slope of the piezoresponse amplitude (= vertical deflection × sensitivity) versus modulation voltage amplitude is determined as the effective piezoelectric coefficient d_{eff}, which has been widely used in piezoelectric oxides and 2D materials[9, 43-45]. Different colors for each point are used to show the d_{eff} value according to the scale bar. The highest d_{eff} value is observed in the freestanding film with *c*/*a* domain structure. Besides, in order to obtain the accurate d_{33} of each film, we use the PMN-PT single crystal with known piezoelectric coefficient for calibration (Fig. S11). The average d_{33} value for *c*/*a* domain structure film is 214.1 pm/V, compared to 86.3 pm/V for *c*-dominated domain structure film, implying a × 2.5 increased in d_{33} (Fig. 4g), which is also consistent with results of phase-field simulations (Fig. 1b). To the best of our knowledge, this value is higher than ever reported for 2D ferroelectric systems (Fig. S12).

In summary, we propose an aftergrowth thermal treatment to tune the longitudinal piezoelectricity in freestanding PTO membrane by manipulating the domain structures. Moreover, a systematic investigation on the domain structures and the corresponding piezoelectric coefficients d_{33} in freestanding PTO film is carried out using phase-field simulations, exhibiting the feasibility of tuning piezoelectricity through domain structure engineering. In our experiments, the domain engineering from *c*-dominated domain to *c*/*a* domain and *a* domain can be realized by controlling the key parameter of cooling rate and all the annealed freestanding films preserve a relatively good ferroelectricity. Significantly, our result shows a substantial enhancement of

longitudinal piezoelectric coefficients d_{33} in freestanding PTO film with *c*/*a* domain structure (~ 214 pm/V). Our work provides a new route to tune and enhance the piezoelectric properties of low-dimensional ferroelectric perovskites for potential electronic applications.

MATERIALS AND METHODS

Deposition of epitaxial thin films. The water-soluble SAO layer was grown first on (001) STO single-crystalline substrate followed by the growth of a thin film PTO by Oxide MBE system. The SAO films were grown with an oxidant (10% O^3 and 90% O^2) background partial pressure of oxygen p_{O2} of 1×10^{-6} Torr and at a substrate temperature $T_{substrate}$ =950°C. The SAO and PTO films were grown layer by layer, for each of which the thickness was monitored by reflection high-energy electron diffraction (RHEED) oscillations. The PTO films were grown with an oxidant (distilled O_3) background pressure of 2×10^{-5} Torr and at $T_{substrate}$=625°C. Due to the volatility of lead, PTO films were grown in adsorption-controlled mode with a fixed Pb:Ti flux ratio of 13:1 and the thickness was controlled by deposition time of titanium.

Release and transfer PTO films. To transfer the freestanding film to silicon, a supporting layer of PMMA (AR-P 672.02) were spin-coated onto PTO film surface. In order to make it easier to float up and manipulate, a frame-shaped PET (polyethylene terephthalate) membrane is then attached on PMMA layer. Heating to solidify PMMA. They were then immersed into deionized water at room temperature for 24 hours in order to dissolving the SAO layer completely. The PTO film with support layers were separated from the STO substrate and then transferred on silicon. Finally, after dissolving PMMA in acetone, the bare freestanding PTO film remained on silicon by removed the frame.

Structural Characterization. The crystal structure was examined by a high-resolution single crystal X-ray diffractometer using a Bruker D8 Discover instrument. The incident X-ray was from Cu-Kα emission and had a wavelength of 1.5418 Å.

Atomic-resolution STEM-HAADF images were obtained on a double spherical aberration-corrected STEM/TEM FEI Titan G2 60-300 at 300 kV with a field emission gun. The probe convergence angle on the Titan electron microscope was 22.5 mrad, and the angular range of the HAADF detector was from 79.5 mrad to 200 mrad.

Piezoresponse Force Microscopy Measurements. The local ferroelectric properties were measured on freestanding films on a conducting Si wafer using an Asylum Research MFP-3D Origin+ SPM scanning probe microscope. Olympus AC240TM Pt/Ti-coated tip (2 N m^{-1} in force constant) were used in the PFM measurements. Hysteresis loops were collected in the dual AC resonance tracking (DART) mode. PFM images were taken in the DART mode with driving voltage (1 V a.c.) applied at the tip. During the domain writing, the voltage was also applied at the tip.

X-ray Photoemission Spectroscopy Measurements. The XPS spectra were collected at room temperature with a Thermo Scientific K-Alpha instrument using Al Kα radiation (hν = 1486.6 eV). The pass energy and step size are set at 50 and 0.1 eV, respectively. The flood gun was used during all experiments to prevent possible charging effect, and the main peak position of C 1s (284.8 eV) is used for minor binding energy calibration for all measured spectra.

Phase Field Modeling. In the phase-field simulation of freestanding PTO film, the domain structure can be obtained by solving the time-dependent Landau–Ginzburg–Devonshire equations[46]

$$\frac{\partial P_i(\mathbf{r},t)}{\partial t} = -L\frac{\delta F}{\delta P_i(\mathbf{r},t)}, \ (i=3), \tag{1}$$

where L is the kinetic coefficient, F is the total free energy of the system, r is the space position and $P_i(\mathrm{r}, t)$ is the polarization. $\frac{\delta F}{\delta P_i(\mathbf{r},t)}$ is the thermodynamic driving force for the spatial and temporal evolution of polarization.

The total free energy of the system includes the bulk free energy f_{bulk}, elastic energy f_{elas}, electrostatic energy f_{elec} and gradient energy f_{grad}:

$$F = \int_V (f_{\mathrm{bulk}} + f_{\mathrm{elas}} + f_{\mathrm{elec}} + f_{\mathrm{grad}})\mathrm{dV}, \tag{2}$$

where V is the system volume. Detailed expressions for each of the energy density contributions, and the material constants for $PbTiO_3$ used in the simulations are collected from the reported literatures[46, 47].

In the simulations, we employed 150×150×50 uniform discrete grid points to the 3D system, and the grid space in real space is chosen to be $\Delta x_1 = \Delta x_2 = 2$ nm and $\Delta x_3 = 1$ nm. The periodic boundary conditions were applied in the in-plane direction (x_1 and x_2 axes). To solve the force equilibrium equations, the mechanical boundary condition was set based on the variety in averaged in-plane lattice constant of the films with ferroelectric phase relative to one with paraelectric phase. The averaged in-plane lattice constant is larger for the films annealed with lower cooling rate. Random noise was used as the initial setup to simulate the thermal fluctuation during the annealing process. The stable domain structure at equilibrium was obtained by minimizing the total free energy of the system by iteratively solving the time-dependent Ginzburg–Landau equation (i.e. Eq. (1)). Each of stable domain structure was then used to evaluate their piezoelectricity. A small external electrical field of 1 kV/cm was applied quasistatically along the thickness direction to induce piezoelectric strain. The piezoelectric coefficient d_{33} can be obtained by dividing the average piezoelectric strain with the applied electrical field[48].

FIGURES

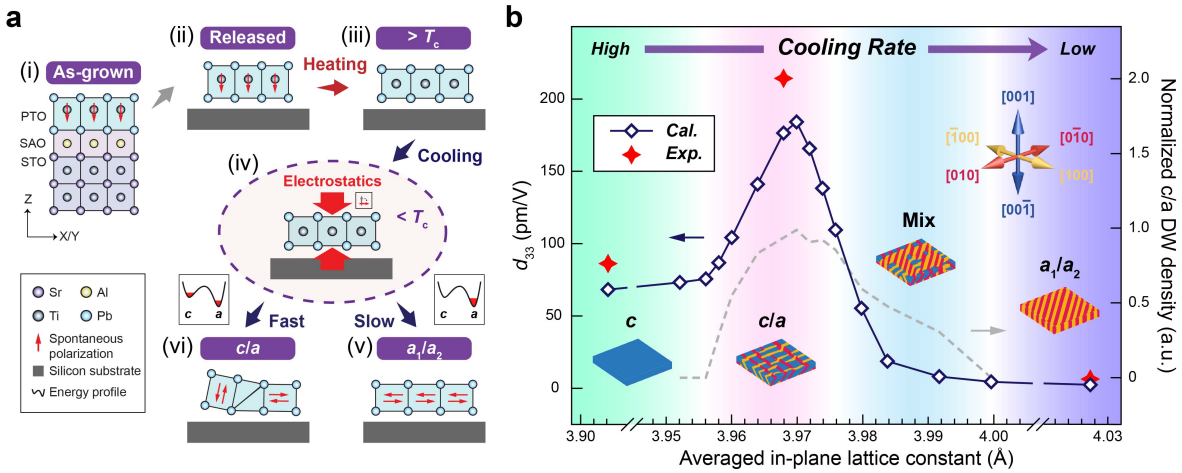

Figure 1. Concept of the aftergrowth thermal treatment to obtain different domain structures predicted by the phase-field simulations. a, Illustration of mechanism about the domain formation vs cooling rate. Transferring process barely affects domain structure in freestanding PTO films (i, ii). After heated to higher temperature (> T_c), it undergoes a transition from ferroelectric tetragonal phase to paraelectric cubic phase (iii). Once the temperature is lower than T_c, electrostatics forces the polarization to the in-plane (iv). If cooling rate is low enough, all the polarization forms in the in-plane direction (v); while cooling rate is high, *c*/*a* domain structure forms (vi). **b,** Domain structures and piezoelectric coefficients d_{33} (dark blue diamonds) predicted by the phase-field simulations. Corresponding experimental results (red solid stars). Normalized *c*/*a* domain wall density within the constituent domain structure (dashed grey line).

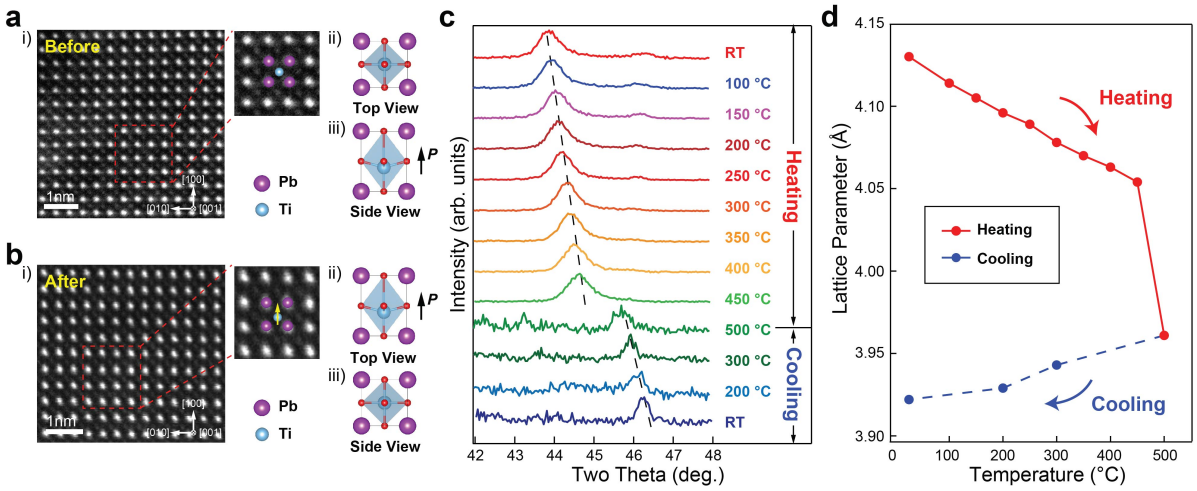

Figure 2. Evolution of domain structures in 50 nm freestanding PTO. a, b, i) Plane-view HAADF images of PTO film before (a) and after (b) annealing the film, showing the polarization along the [001] direction and [100] direction, respectively. The magnifications of red rectangular area (purple: Pb^{2+}, blue: Ti^{4+}). ii) Projection of the unit-cell along the [001] direction. iii) Projection of the unit-cell along the [100] direction. **c,** Temperature-dependent HRXRD 2θ-ω scans of the PTO (002) peak of freestanding PTO film during heating (25 to 500°C) and slow cooling (500 to 25°C) processes. The black dashed lines denote the peak shift across the phase transition. **d,** Temperature-dependent OOP lattice parameters of PTO films during annealing processes.

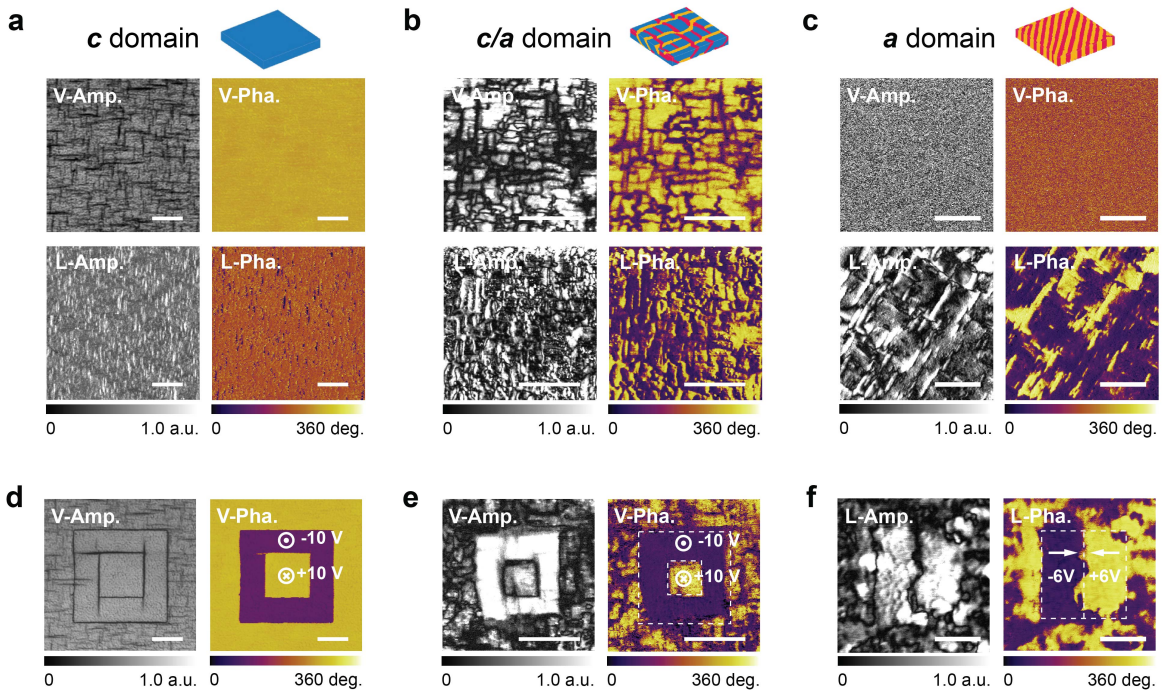

Figure 3. Three typical domain structures and corresponding switching behaviors in freestanding PTO film. a, *c*-dominated domain. **b,** *c*/*a* domain. **c,** *a* domain. VPFM amplitude (V-Amp.), VPFM phase (V-Pha.), LPFM amplitude (L-Amp.) and LPFM phase (L-Pha.) images. Amplitude and phase images of **d** *c*-dominated domain and **e** *c*/*a* domain freestanding film after written a box-in-box pattern. **f,** Amplitude and phase images of *a* domain freestanding film after in-plane domain switching via trailing field. Scale bar, 1 um.

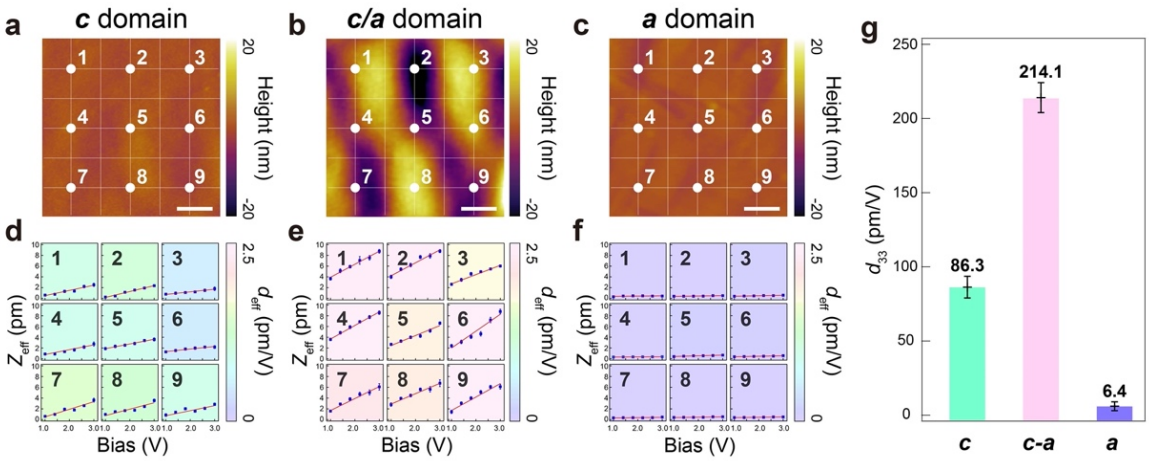

Figure 4. Probing the electromechanical response in PTO freestanding films with three different domain structures. a-c, Topography images of *c*-dominated, *c*/*a* and *a* domain structures, respectively. **d-f,** Representative piezoelectric displacement (Z_{eff}) of 9 array points on the freestanding films, as functions of the applied AC tip bias. The red solid line indicates fitting line obtained by the least-square method. Effective piezoelectric coefficients d_{eff} of each point retrieved from the fitting line slopes. **g,** Average piezoelectric coefficients d_{33} of each sample calibrated by PMN-PT crystal with known piezoelectric coefficients. Note the clear enhancement of d_{33} for the *c*/*a* domain structure sample. Scale bar, 600 nm.

ASSOCIATED CONTENT

The following files are available free of charge.

Supplementary Information (PDF) : Additional experimental details, materials, and methods, including photographs of experimental setup

AUTHOR INFORMATION

Corresponding Author

*Correspondence to: hongjw@bit.edu.cn, ynie@nju.edu.cn

Author Contributions

The manuscript was written through contributions of all authors. All authors have given approval to the final version of the manuscript. ‡These authors contributed equally.

ACKNOWLEDGMENT

This work was supported by the National Key Projects for Research and Development of China (Grant Nos. 2021YFA1400400, 2021YFA1400300), the National Natural Science Foundation of China (Grant Nos. 1861161004, 12172047, 11874199 and 52102133), Beijing Natural Science Foundation (Grant No. Z190011), China National Postdoctoral Program for Innovative Talents (Grant No. BX20220147) and the Fundamental Research Funds for the Central Universities (grant 0213-14380221). Theoretical calculations were performed using resources of the Supercomputer Centre in Chongqing.

REFERENCES

1. Fu, H.; Cohen, R. E., Polarization rotation mechanism for ultrahigh electromechanical response in single-crystal piezoelectrics. *Nature* **2000,** *403*, 281-283.

2. Zhang, S.; Li, F.; Jiang, X.; Kim, J.; Luo, J.; Geng, X., Advantages and challenges of relaxor-$PbTiO_3$ ferroelectric crystals for electroacoustic transducers – A review. *Prog. Mater. Sci.* **2015,** *68*, 1-66.

3. Kingon, A. I.; Srinivasan, S., Lead zirconate titanate thin films directly on copper electrodes for ferroelectric, dielectric and piezoelectric applications. *Nat. Mater.* **2005,** *4*, 233-237.

4. Yang, R.; Qin, Y.; Dai, L.; Wang, Z. L., Power generation with laterally packaged piezoelectric fine wires. *Nat. Nanotechnol.* **2009,** *4*, 34-39.

5. Wang, Z. L.; Song, J., Piezoelectric Nanogenerators Based on Zinc Oxide Nanowire Arrays. *Science* **2006,** *312*, 242-246.

6. Xu, B.; Zhang, P.; Zhu, J.; Liu, Z.; Eichler, A.; Zheng, X.-Q.; Lee, J.; Dash, A.; More, S.; Wu, S.; Wang, Y.; Jia, H.; Naik, A.; Bachtold, A.; Yang, R.; Feng, P. X. L.; Wang, Z., Nanomechanical Resonators: Toward Atomic Scale. *ACS Nano* **2022,** *16*, 15545-15585.

7. Zhu, H.; Wang, Y.; Xiao, J.; Liu, M.; Xiong, S.; Wong, Z. J.; Ye, Z.; Ye, Y.; Yin, X.; Zhang, X., Observation of piezoelectricity in free-standing monolayer MoS_2. *Nat. Nanotechnol.* **2015,** *10*, 151-155.

8. Wu, W.; Wang, L.; Li, Y.; Zhang, F.; Lin, L.; Niu, S.; Chenet, D.; Zhang, X.; Hao, Y.; Heinz, T. F.; Hone, J.; Wang, Z. L., Piezoelectricity of single-atomic-layer MoS_2 for energy conversion and piezotronics. *Nature* **2014,** *514*, 470-474.

9. Rogée, L.; Wang, L.; Zhang, Y.; Cai, S.; Wang, P.; Chhowalla, M.; Ji, W.; Lau, S. P., Ferroelectricity in untwisted heterobilayers of transition metal dichalcogenides. *Science* **2022,** *376*, 973-978.

10. Li, F.; Lin, D.; Chen, Z.; Cheng, Z.; Wang, J.; Li, C.; Xu, Z.; Huang, Q.; Liao, X.; Chen, L.-Q.; Shrout, T. R.; Zhang, S., Ultrahigh piezoelectricity in ferroelectric ceramics by design. *Nat. Mater.* **2018,** *17*, 349-354.

11. Lee, M.; Renshof, J. R.; van Zeggeren, K. J.; Houmes, M. J. A.; Lesne, E.; Šiškins, M.; van Thiel, T. C.; Guis, R. H.; van Blankenstein, M. R.; Verbiest, G. J.; Caviglia, A. D.; van der Zant, H. S. J.; Steeneken, P. G., Ultrathin Piezoelectric Resonators Based on Graphene and Free-Standing Single-Crystal $BaTiO_3$. *Adv. Mater.* **2022,** *34*, 2204630.

12. Lu, D.; Baek, D. J.; Hong, S. S.; Kourkoutis, L. F.; Hikita, Y.; Hwang, Harold Y., Synthesis of freestanding single-crystal perovskite films and heterostructures by etching of sacrificial water-soluble layers. *Nat. Mater.* **2016,** *15*, 1255-1260.

13. Ji, D.; Cai, S.; Paudel, T. R.; Sun, H.; Zhang, C.; Han, L.; Wei, Y.; Zang, Y.; Gu, M.; Zhang, Y.; Gao, W.; Huyan, H.; Guo, W.; Wu, D.; Gu, Z.; Tsymbal, E. Y.; Wang, P.; Nie, Y.; Pan, X., Freestanding crystalline oxide perovskites down to the monolayer limit. *Nature* **2019,** *570*, 87-90.

14. Ahart, M.; Somayazulu, M.; Cohen, R. E.; Ganesh, P.; Dera, P.; Mao, H.-k.; Hemley, R. J.; Ren, Y.; Liermann, P.; Wu, Z., Origin of morphotropic phase boundaries in ferroelectrics. *Nature* **2008,** *451*, 545-548.

15. Guo, R.; Cross, L. E.; Park, S. E.; Noheda, B.; Cox, D. E.; Shirane, G., Origin of the High Piezoelectric Response in $PbZr_{1-x}Ti_xO_3$. *Phys. Rev. Lett.* **2000,** *84*, 5423-5426.

16. Zeches, R. J.; Rossell, M. D.; Zhang, J. X.; Hatt, A. J.; He, Q.; Yang, C.-H.; Kumar, A.; Wang, C. H.; Melville, A.; Adamo, C.; Sheng, G.; Chu, Y.-H.; Ihlefeld, J. F.; Erni, R.; Ederer, C.; Gopalan, V.; Chen, L. Q.; Schlom, D. G.; Spaldin, N. A.; Martin, L. W.; Ramesh, R., A Strain-Driven Morphotropic Phase Boundary in $BiFeO_3$. *Science* **2009,** *326*, 977-980.

17. Damodaran, A. R.; Liang, C.-W.; He, Q.; Peng, C.-Y.; Chang, L.; Chu, Y.-H.; Martin, L. W., Nanoscale Structure and Mechanism for Enhanced Electromechanical Response of Highly Strained $BiFeO_3$ Thin Films. *Adv. Mater.* **2011,** *23*, 3170-3175.

18. Damodaran, A. R.; Pandya, S.; Agar, J. C.; Cao, Y.; Vasudevan, R. K.; Xu, R.; Saremi, S.; Li, Q.; Kim, J.; McCarter, M. R.; Dedon, L. R.; Angsten, T.; Balke, N.; Jesse, S.; Asta, M.; Kalinin, S. V.; Martin, L. W., Three-State Ferroelastic Switching and Large Electromechanical Responses in $PbTiO_3$ Thin Films. *Adv. Mater.* **2017,** *29*, 1702069.

19. Han, L.; Addiego, C.; Prokhorenko, S.; Wang, M.; Fu, H.; Nahas, Y.; Yan, X.; Cai, S.; Wei, T.; Fang, Y.; Liu, H.; Ji, D.; Guo, W.; Gu, Z.; Yang, Y.; Wang, P.; Bellaiche, L.; Chen, Y.; Wu, D.; Nie, Y.; Pan, X., High-density switchable skyrmion-like polar nanodomains integrated on silicon. *Nature* **2022,** *603*, 63-67.

20. Li, Y.; Zatterin, E.; Conroy, M.; Pylypets, A.; Borodavka, F.; Björling, A.; Groenendijk, D. J.; Lesne, E.; Clancy, A. J.; Hadjimichael, M.; Kepaptsoglou, D.; Ramasse, Q. M.; Caviglia, A. D.; Hlinka, J.; Bangert, U.; Leake, S. J.; Zubko, P., Electrostatically Driven Polarization Flop and Strain-Induced Curvature in Free-Standing Ferroelectric Superlattices. *Adv. Mater.* **2022,** *34*, 2106826.

21. Dong, G.; Li, S.; Yao, M.; Zhou, Z.; Zhang, Y.-Q.; Han, X.; Luo, Z.; Yao, J.; Peng, B.; Hu, Z.; Huang, H.; Jia, T.; Li, J.; Ren, W.; Ye, Z.-G.; Ding, X.; Sun, J.; Nan, C.-W.;

Chen, L.-Q.; Li, J.; Liu, M., Super-elastic ferroelectric single-crystal membrane with continuous electric dipole rotation. *Science* **2019,** *366*, 475-479.

22. Hong Seung, S.; Gu, M.; Verma, M.; Harbola, V.; Wang Bai, Y.; Lu, D.; Vailionis, A.; Hikita, Y.; Pentcheva, R.; Rondinelli James, M.; Hwang Harold, Y., Extreme tensile strain states in $La_{0.7}Ca_{0.3}MnO_3$ membranes. *Science* **2020,** *368*, 71-76.

23. Cai, S.; Lun, Y.; Ji, D.; Lv, P.; Han, L.; Guo, C.; Zang, Y.; Gao, S.; Wei, Y.; Gu, M.; Zhang, C.; Gu, Z.; Wang, X.; Addiego, C.; Fang, D.; Nie, Y.; Hong, J.; Wang, P.; Pan, X., Enhanced polarization and abnormal flexural deformation in bent freestanding perovskite oxides. *Nat. Commun.* **2022,** *13*, 5116.

24. Schlom, D. G.; Chen, L.-Q.; Fennie, C. J.; Gopalan, V.; Muller, D. A.; Pan, X.; Ramesh, R.; Uecker, R., Elastic strain engineering of ferroic oxides. *MRS Bulletin* **2014,** *39*, 118-130.

25. Pesquera, D.; Parsonnet, E.; Qualls, A.; Xu, R. J.; Gubser, A. J.; Kim, J.; Jiang, Y. Z.; Velarde, G.; Huang, Y. L.; Hwang, H. Y.; Ramesh, R.; Martin, L. W., Beyond Substrates: Strain Engineering of Ferroelectric Membranes. *Adv. Mater.* **2020,** *32*, 2003780.

26. Han, L.; Fang, Y.; Zhao, Y.; Zang, Y.; Gu, Z.; Nie, Y.; Pan, X., Giant Uniaxial Strain Ferroelectric Domain Tuning in Freestanding $PbTiO_3$ Films. *Adv. Mater. Inter.* **2020,** *7*, 1901604.

27. Wang, J.-J.; Su, Y.-J.; Wang, B.; Ouyang, J.; Ren, Y.-H.; Chen, L.-Q., Strain engineering of dischargeable energy density of ferroelectric thin-film capacitors. *Nano Energy* **2020,** *72*, 104665.

28. Wang, J.-J.; Wang, B.; Chen, L.-Q., Understanding, Predicting, and Designing Ferroelectric Domain Structures and Switching Guided by the Phase-Field Method. *Annu. Rev. Mater. Res.* **2019,** *49*, 127-152.

29. Qiu, C.; Wang, B.; Zhang, N.; Zhang, S.; Liu, J.; Walker, D.; Wang, Y.; Tian, H.; Shrout, T. R.; Xu, Z.; Chen, L.-Q.; Li, F., Transparent ferroelectric crystals with ultrahigh piezoelectricity. *Nature* **2020,** *577*, 350-354.

30. Li, F.; Zhang, S.; Xu, Z.; Chen, L.-Q., The Contributions of Polar Nanoregions to the Dielectric and Piezoelectric Responses in Domain-Engineered Relaxor-$PbTiO_3$ Crystals. *Adv. Funct. Mater.* **2017,** *27*, 1700310.

31. Shirane, G.; Hoshino, S.; Suzuki, K., X-Ray Study of the Phase Transition in Lead Titanate. *Physical Review* **1950,** *80*, 1105-1106.

32. Wada, S.; Tsurumi, T., Enhanced piezoelectricity of barium titanate single crystals with engineered domain configuration. *Br. Ceram. Trans.* **2004,** *103*, 93 - 96.

33. Yun, S.; Song, K.; Chu, K.; Hwang, S.-Y.; Kim, G.-Y.; Seo, J.; Woo, C.-S.; Choi, S.-Y.; Yang, C.-H., Flexopiezoelectricity at ferroelastic domain walls in WO_3 films. *Nat. Commun.* **2020,** *11*, 4898.

34. Davis, M., Picturing the elephant: Giant piezoelectric activity and the monoclinic phases of relaxor-ferroelectric single crystals. *J. Electroceram.* **2007,** *19*, 25-47.

35. Ivry, Y.; Chu, D. P.; Durkan, C., Bundles of polytwins as meta-elastic domains in the thin polycrystalline simple multi-ferroic system PZT. *Nanotechnology* **2010,** *21*, 065702.

36. Catalan, G.; Lubk, A.; Vlooswijk, A. H. G.; Snoeck, E.; Magen, C.; Janssens, A.; Rispens, G.; Rijnders, G.; Blank, D. H. A.; Noheda, B., Flexoelectric rotation of polarization in ferroelectric thin films. *Nat. Mater.* **2011,** *10*, 963-967.

37. Matzen, S.; Nesterov, O.; Rispens, G.; Heuver, J. A.; Biegalski, M.; Christen, H. M.; Noheda, B., Super switching and control of in-plane ferroelectric nanodomains in strained thin films. *Nat. Commun.* **2014,** *5*, 4415.

38. Crassous, A.; Sluka, T.; Tagantsev, A. K.; Setter, N., Polarization charge as a reconfigurable quasi-dopant in ferroelectric thin films. *Nat. Nanotechnol.* **2015,** *10*, 614-618.

39. Kalinin, S. V.; Bonnell, D. A., Imaging mechanism of piezoresponse force microscopy of ferroelectric surfaces. *Phys. Rev. B* **2002,** *65*, 125408.

40. Zhao, M.; Wang, Z. L.; Mao, S. X., Piezoelectric Characterization of Individual Zinc Oxide Nanobelt Probed by Piezoresponse Force Microscope. *Nano Lett.* **2004,** *4*, 587-590.

41. Qi, Y.; Jafferis, N. T.; Lyons, K.; Lee, C. M.; Ahmad, H.; McAlpine, M. C., Piezoelectric Ribbons Printed onto Rubber for Flexible Energy Conversion. *Nano Lett.* **2010,** *10*, 524-528.

42. Paull, O.; Xu, C.; Cheng, X.; Zhang, Y.; Xu, B.; Kelley, K. P.; de Marco, A.; Vasudevan, R. K.; Bellaiche, L.; Nagarajan, V.; Sando, D., Anisotropic epitaxial stabilization of a low-symmetry ferroelectric with enhanced electromechanical response. *Nat. Mater.* **2022,** *21*, 74-80.

43. Kvasov, A.; McGilly, L. J.; Wang, J.; Shi, Z.; Sandu, C. S.; Sluka, T.; Tagantsev, A. K.; Setter, N., Piezoelectric enhancement under negative pressure. *Nat. Commun.* **2016,** *7*, 12136.

44. Han, S. A.; Kim, T.-H.; Kim, S. K.; Lee, K. H.; Park, H.-J.; Lee, J.-H.; Kim, S.-W., Point-Defect-Passivated MoS_2 Nanosheet-Based High Performance Piezoelectric Nanogenerator. *Adv. Mater.* **2018,** *30*, 1800342.

45. Khan, H.; Mahmood, N.; Zavabeti, A.; Elbourne, A.; Rahman, M. A.; Zhang, B. Y.; Krishnamurthi, V.; Atkin, P.; Ghasemian, M. B.; Yang, J.; Zheng, G.; Ravindran, A. R.; Walia, S.; Wang, L.; Russo, S. P.; Daeneke, T.; Li, Y.; Kalantar-Zadeh, K., Liquid metal-based synthesis of high performance monolayer SnS piezoelectric nanogenerators. *Nat. Commun.* **2020,** *11*, 3449.

46. Li, Y. L.; Hu, S. Y.; Liu, Z. K.; Chen, L. Q., Phase-field model of domain structures in ferroelectric thin films. *Appl. Phys. Lett.* **2001,** *78*, 3878-3880.

47. Chen, W.; Zheng, Y.; Feng, X.; Wang, B., Utilizing mechanical loads and flexoelectricity to induce and control complicated evolution of domain patterns in ferroelectric nanofilms. *J. Mech. Phys. Solids* **2015,** *79*, 108-133.

48. Wang, B.; Li, F.; Chen, L.-Q., Inverse Domain-Size Dependence of Piezoelectricity in Ferroelectric Crystals. *Adv. Mater.* **2021,** *33*, 2105071.

TOC GRAPHIC

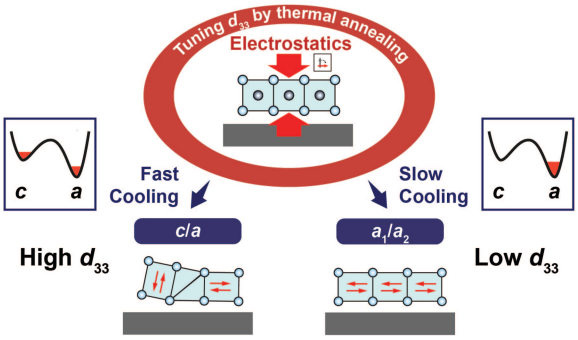
Tuning d_{33} by thermal annealing
Electrostatics
c a
Fast Cooling
Slow Cooling
c a
c/a
a_1/a_2
High d_{33}
Low d_{33}